nanomaterials

MDPI

Article

First-Principles Dynamics Investigation of Germanium as an Anode Material in Multivalent-Ion Batteries

Chaewon Kim, Useul Hwang, Sangjin Lee * and Young-Kyu Han *

Department of Energy and Materials Engineering, Dongguk University-Seoul, Seoul 04620, Republic of Korea; twinstees@dongguk.edu (C.K.); bbohyunh@gmail.com (U.H.)

* Correspondence: dltkdwls@dongguk.edu (S.L.); ykenergy@dongguk.edu (Y.-K.H.)

Abstract: Germanium, a promising electrode material for high-capacity lithium ion batteries (LIBs) anodes, attracted much attention because of its large capacity and remarkably fast charge/discharge kinetics. Multivalent-ion batteries are of interest as potential alternatives to LIBs because they have a higher energy density and are less prone to safety hazards. In this study, we probed the potential of amorphous Ge anodes for use in multivalent-ion batteries. Although alloying Al and Zn in Ge anodes is thermodynamically unstable, Mg and Ca alloys with Ge form stable compounds, $Mg_{2.3}Ge$ and $Ca_{2.4}Ge$ that exhibit higher capacities than those obtained by alloying Li, Na, or K with Ge, corresponding to 1697 and 1771 mA·h·g^{-1}, respectively. Despite having a slightly lower capacity than Ca–Ge, Mg–Ge shows an approximately 150% smaller volume expansion ratio (231% vs. 389%) and three orders of magnitude higher ion diffusivity (3.0×10^{-8} vs. 1.1×10^{-11} cm^2 s^{-1}) than Ca–Ge. Furthermore, ion diffusion in Mg–Ge occurs at a rate comparable to that of monovalent ions, such as Li^+, Na^+, and K^+. The outstanding performance of the Mg–Ge system may originate from the coordination number of the Ge host atoms and the smaller atomic size of Mg. Therefore, Ge anodes could be applied in multivalent-ion batteries using Mg^{2+} as the carrier ion because its properties can compete with or surpass monovalent ions. Here, we report that the maximum capacity, volume expansion ratio, and ion diffusivities of the alloying electrode materials can be understood using atomic-scale structural properties, such as the host–host and host–ion coordination numbers, as valuable indicators.

Keywords: germanium; multivalent-ion battery; magnesium; volume expansion; anode material

Citation: Kim, C.; Hwang, U.; Lee, S.; Han, Y.-K. First-Principles Dynamics Investigation of Germanium as an Anode Material in Multivalent-Ion Batteries. *Nanomaterials* **2023**, *13*, 2868. https://doi.org/10.3390/nano13212868

Academic Editors: Yuhua Duan and J. Woods Halley

Received: 4 October 2023
Revised: 27 October 2023
Accepted: 28 October 2023
Published: 30 October 2023

1. Introduction

Advancements in electrochemical energy storage technology led to extensive research on various systems, such as lithium-ion batteries, Li–S batteries, Li–Se batteries, aqueous ammonium-ion batteries, aqueous Zn-ion batteries, and supercapacitors [1–7]. Among these, multivalent-ion batteries (MIBs) are receiving considerable attention as promising alternatives to lithium-ion batteries (LIBs), owing to their earth abundance and cost efficiency. The ability of divalent (Mg^{2+}, Ca^{2+}, and Zn^{2+}) and trivalent (Al^{3+}) ions to transfer more than one electron allows them to store more energy in batteries than is possible with monovalent LIBs [8–10]. Moreover, double- or triple-electron exchange per ion during the electrochemical reaction could potentially yield higher specific energy densities [8,11]. Metal negative electrodes such as Al, Mg, Ca, and Zn are considered extremely favorable since they can provide remarkably high gravimetric (820–2980 mA·h·g^{-1}) and volumetric capacities (2073–8046 mA·h·cm^{-3}), which are substantially higher than the 372 mA·h·g^{-1} and 818 mA·h·cm^{-3}, respectively, of the graphite anode used in commercial LIBs [11–16]. However, using metal anodes presents several unfavorable issues, including sluggish ion diffusion kinetics in both the electrolyte and electrodes, instability of the electrodes, formation of a complicated solid electrolyte interface, and self-corrosion of the anodes [17–19]. Certain anode materials, such as titanium oxides and vanadium oxides were investigated

based on their intercalation reactions [20,21]; however, research on anodes for MIBs remains challenging compared to that on cathodes. Despite the promise of emerging materials, such as organic electrodes [22] and structure-engineered composites [23], which have advantages that include flexibility in design and a wide range of property tunabilities, the practical implementation of MIBs was hindered by inherent challenges, including relatively low redox potentials, and insufficient electronic and ionic conductivities.

One material that was widely investigated as a highly promising material for the next generation of anodes in LIBs is germanium (Ge) [21,24–27] because of its high specific capacity (1624 and 1384 $mA{\cdot}h{\cdot}g^{-1}$ for $Li_{22}Ge_5$ and $Li_{15}Ge_4$ alloys, respectively [28]), superb rate performance, and good cycling reliability due to its fast kinetics for both Li^+ ion diffusion and electronic conduction [27,29–31]. However, as with other alloy-based materials used in negative electrodes in LIBs, Ge undergoes large volume changes in the fully lithiated state of $Li_{22}Ge_5$. Numerous strategies were suggested to overcome this problem [25,32], and these strategies will likely enhance the electrochemical performance of Ge anode materials in LIBs in the near future.

Both Ge and Si anodes received significant attention as next-generation LIB anodes. They share several similarities, including the obstacle of having a large volume expansion ratio upon lithiation, which can result in capacity fading. However, Ge anodes have several advantages over Si anodes. First, the capacity of Ge is only half that of Si (1624 vs. 3579 $mA{\cdot}h{\cdot}g^{-1}$); however, it has a higher density (5.30 vs. 2.30 $g{\cdot}cm^{-1}$), which endows it with a charge stored per volume similar to that of Si [25,33]. Second, the Li-ion diffusivity is two orders of magnitude quicker for Ge (at room temperature, 6.51×10^{-12} vs. 1.41×10^{-14} $cm^2{\cdot}s^{-1}$) than for Si. Third, the electronic conductivity is three orders of magnitude higher for Ge than for Si (2.1 vs. 1.6×10^{-3} $S{\cdot}m^{-1}$) [34,35]. Thus, an analysis of the advantages of Ge anodes is essential for the development of next-generation LIB anodes.

Exploring amorphous Ge anodes for MIBs is also a worthwhile research endeavor. While a low reversible capacity less than 350 $mA{\cdot}h{\cdot}g^{-1}$ was reported for the crystalline Ge anode in Na-ion batteries [36], our group theoretically suggested [37,38] that Ge becomes reactive toward Na ions when its amorphous phase is adopted, thereby providing a maximum capacity of 576 $mA{\cdot}h{\cdot}g^{-1}$ at $Na_{1.56}Ge$. After the publication of our computational results, several experimental studies [39,40] performed on amorphous Ge anodes reported initial reversible capacities of $\leq$430 $mA{\cdot}h{\cdot}g^{-1}$.

Considering the studies on Na-ion batteries, amorphous Ge may be a promising candidate for utilization as the anode in MIBs, as it has the potential to offer higher capacities than crystalline Ge. However, the diffusion kinetics are poorer for multivalent ions than for Li ions owing to the stronger coulombic interactions between multivalent carrier ions and the electrode material [41,42]. This sluggish and poor diffusion of multivalent ions was primarily observed in crystalline electrodes, particularly in metal oxides, such as Ni_2O_4, Mn_2O_4, TiO_2, and $K_xW_3O_9$ [10]. We believe that higher ion diffusivity will be achieved with amorphous Ge than with crystalline Ge. Unlike crystalline Ge, amorphous Ge does not have long-range order [43,44]; therefore, it can accelerate the structural opening of the localized transport pathway through which multivalent ions migrate.

First-principles molecular dynamics (FPMD) simulations can provide atomistic structural descriptions of amorphous materials with precision at the quantum mechanical level. This enables the derivation of specific values for several parameters, such as atomic coordination numbers, bond angles, and interatomic distances in the structures of amorphous materials, which are difficult to determine experimentally. This distinctive information can be applied to examine the diffusion properties and reaction processes of carrier ions in amorphous electrodes using FPMD simulations. FPMD simulations were used by our group to provide a clear description of amorphous negative electrodes, such as crystalline Si/amorphous Li_xSi interfaces [45], amorphous Si anodes for Na [37], K [46], and Mg [47], and amorphous Al_2O_3 interfaces for Li and Na [48,49]. In addition, we were able to reproduce and provide a reasonable explanation for the findings of several experimental studies on these systems [50–52]. Assessing the electrochemical performance by investigating the

reactions of amorphous Ge materials with various multivalent ions via FPMD simulations may provide experimental researchers with research strategies for fabricating MIB anodes.

We performed FPMD simulations to gain insights into the chemical bonding and structural changes that occur when amorphous Ge material alloys with the multivalent Mg^{2+} and Ca^{2+} cations. We found that the Mg–Ge and Ca–Ge alloys were most stable at compositions of $Mg_{2.3}Ge$ and $Ca_{2.4}Ge$, respectively, and showed the highest capacities of 1697 and 1771 $mA{\cdot}h{\cdot}g^{-1}$, respectively. Although the $Mg_{2.3}Ge$ alloy has a slightly lower specific capacity than $Ca_{2.4}Ge$ (~4%), it exhibits a ~150% smaller volume expansion ratio and a three orders of magnitude-higher ion diffusivity than $Ca_{2.4}Ge$, while demonstrating comparable or superior values to those of $Li_{4.0}Ge$, $Na_{1.5}Ge$, and $K_{1.2}Ge$. We found that the values of the average coordination numbers of $CN_{host–host}$ and $CN_{host–ion}$ are decisive descriptors for comprehending the specific capacity, volume expansion, and ion diffusivity of alloy-based negative electrode materials. The findings of this study suggest that the Mg^{2+} cation has the highest potential among the multivalent ions for use as a promising carrier ion in Ge anodes, and the performance of Mg–Ge alloys is comparable to that of monovalent ions.

2. Computational Details

First-principles density functional theory (DFT) computations were carried out as implemented in the Vienna ab initio simulation package (VASP). The Perdew–Burke–Ernzerhof (PBE) exchange and correlation functionals and the projector augmented wave (PAW) method were adopted. The valence electron configurations considered for Li, Na, K, Al, Mg, Ca, Zn, and Ge were $1s^2 2s^1$, $2p^6 3s^1$, $3p^6 4s^1$, $3s^2 3p^1$, $2p^6 3s^2$, $3p^6 4s^2$, $3d^{10} 4s^2$, and $4s^2 4p^2$, respectively. In our study, we constructed a periodic cubic super cell with 40 Ge atoms $40 \times x$ M atoms for each amorphous M_xGe (M = Li, Na, K, Mg, Al, Ca, and Zn) structure. A $3 \times 3 \times 3$ k-point mesh was used for the Brillouin zone integration. The simulation procedure for amorphous M_xGe (M = Li, Na, K, Mg, Ca, Zn, and Al) alloys consists of two steps: (1) volume relaxation and (2) energy evaluation. First, for a given ion concentration (x), the volume of M_xGe was determined using the liquid quench method. Initially, the cubic supercells containing $40 \times x$ M and 40 Ge atoms were randomly generated with estimated dimensions. This structure underwent a heating process (up to 2000 K, 1 $K{\cdot}fs^{-1}$), followed by equilibration (at 2000 K for 3 ps), and was finally quenched (down to 300 K, 1 $K{\cdot}fs^{-1}$) [53,54]. The quenched structure was equilibrated for an additional 5 ps at 300 K (Figure S1). From the last 2 ps of the equilibrating run, five structures were picked for every 500 computation steps (Figure S1) and then fully relaxed until the atomic position, supercell shape, and supercell volume were optimized as the residual force converged within 0.03 $eV{\cdot}Å^{-1}$. In this step, the plane-wave kinetic energy was augmented by 30% to mitigate the Pulay stress problem [55]. The detailed FPMD simulation procedure is included in the Supporting Information.

For amorphous Ge, the computed physical and chemical properties are in close accordance with those reported in previous studies. The formation energy is 0.11 eV higher per Ge atom for amorphous Ge than for crystalline Ge. The predicted density of amorphous Ge (5.57 $g{\cdot}cm^{-3}$) is comparable to the experimental result (5.32 $g{\cdot}cm^{-3}$ [33]). The simulated Ge–Ge bond length (2.46 Å), analyzed by the radial distribution functions (RDFs), is consistent with 2.3–2.5 Å in theoretical [56] and experimental studies [57,58]. The agreement between the calculated and experimental results supports the accuracy of the amorphous structures obtained from our FPMD simulations.

3. Results and Discussion

Mg–Ge, Ca–Ge, Al–Ge, and Zn–Ge amorphous alloys were generated using FPMD simulations. Figure 1 shows the formation energies of amorphous Mg_xGe, Ca_xGe, Al_xGe, and Zn_xGe ($0.0 \leq x \leq 5.0$) calculated with a reference to an amorphous Ge electrode. The formation energies were positive for the Zn–Ge, and Al–Ge alloys, whereas those for the Mg–Ge, Ca–Ge, Li–Ge, Na–Ge, and K–Ge alloys had negative values. These results indicate

that the electrochemical reactions required for Mg^{2+}, Ca^{2+}, Li^{+}, Na^{+}, and K^{+} ions to form alloys in amorphous Ge are thermodynamically favorable, whereas Zn^{2+} and Al^{3+} cannot alloy stably with amorphous Ge. The alloys with negative formation energies, such as the Mg–Ge, Ca–Ge, Li–Ge, Na–Ge, and K–Ge alloys, were also thermodynamically favorable against separation into Mg, Ca, Li, Na, and K metals and the Ge anode. The amorphous alloys of Mg–Ge and Ca–Ge that had the most stable ion concentration were $Mg_{2.3}Ge$ and $Ca_{2.4}Ge$, corresponding to formation energies of −0.56 and −1.94 eV, respectively, and had high capacities of 1697 and 1771 $mA{\cdot}h{\cdot}g^{-1}$, respectively.

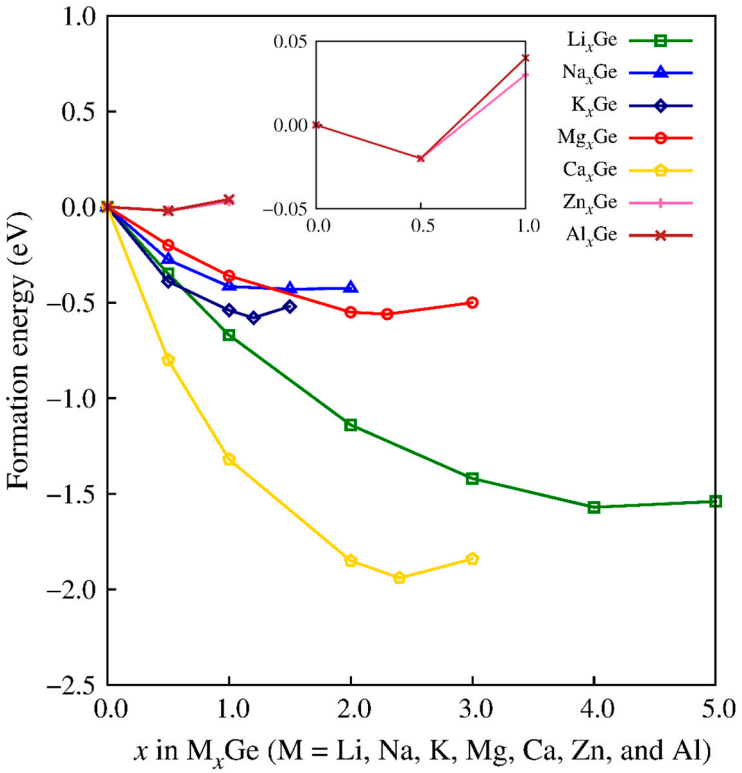

Figure 1. Formation energies of the M_xGe (M = Li, Na, K, Al, Mg, Ca, and Zn) amorphous alloys.

We also compared the formation energies of Ge alloyed with divalent Mg^{2+} and Ca^{2+} to those of Ge alloyed with monovalent ions, as shown in Figure 1. The most stable ion concentrations for $Li_{4.0}Ge$, $Na_{1.5}Ge$, and $K_{1.2}Ge$ corresponded to formation energies of −1.57, −0.40, and −0.58 eV, respectively. The concentration of Li (x = 4.0) at the most stable state agreed well with previously reported Ge electrodes for lithium [24,34]. While a sufficiently low formation energy for metal electrode alloys is crucial to guarantee a high redox potential, high ion concentrations are also critical for batteries to provide sufficient capacities. The calculated specific capacities of the Li–Ge, Na–Ge, and K–Ge alloys were 1476, 553, and 443 $mA{\cdot}h{\cdot}g^{-1}$, respectively, showing that the Li–Ge alloy had the highest capacity. Despite the relatively low stability and capacities of the Na–Ge and K–Ge alloys compared to those of the Li–Ge alloy, the negative formation energies would still enable Na^{+} and K^{+} ions to favorably alloy with Ge. The formation energies of the energetically most stable ion concentrations for the M_xGe (M = Mg, Ca, Li, Na, and K) systems suggested that the strength of the driving force for M–Ge alloying has an order of Ca > Li > K ~ Mg > Na. However, a noteworthy point is that the capacities were higher for $Mg_{2.3}Ge$ (1697) and $Ca_{2.4}Ge$ (1771 $mA{\cdot}h{\cdot}g^{-1}$) than for $Li_{4.0}Ge$ (1476 $mA{\cdot}h{\cdot}g^{-1}$).

Figure 2 shows the atomic structures of amorphous M_xGe (M = Mg, Ca, Li, Na, and K) (x = full composition). The compositions of $Mg_{2.3}Ge$ and $Ca_{2.4}Ge$ were generally consistent with the presence of Mg_2Ge and Ca_2Ge crystals in the Mg–Ge and Ca–Ge phase diagrams, respectively [59,60]. The formation energies of $Mg_{2.3}Ge$ and $Ca_{2.4}Ge$ were calculated as

−0.56 and −1.94 eV, respectively, indicating that Ca–Ge alloying was thermodynamically more stable than that of Mg–Ge. Notably, the formation energy for amorphous $Mg_{2.3}Ge$ had a positive value (+0.003 eV) when referenced to crystalline Ge. This result implies that the crystalline Ge electrode was less likely than the amorphous Ge electrode to form the $Mg_{2.3}Ge$ phase.

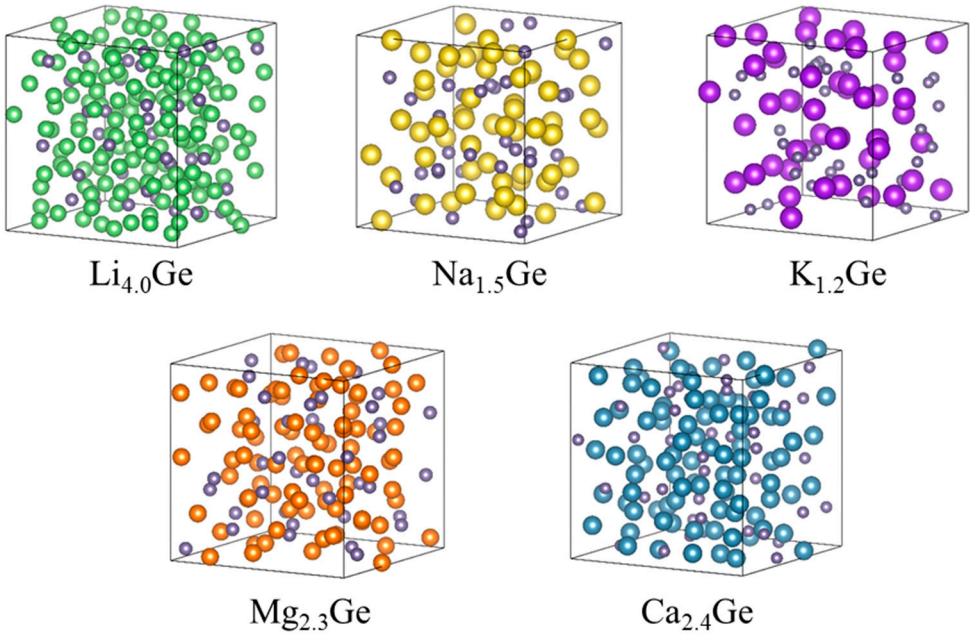

Figure 2. Atomic structures of M_xGe (M = Mg, Ca, Li, Na, and K), where x is at the maximum concentration. Green, yellow, purple, orange, blue, and gray spheres represent Mg, Ca, Li, Na, K, and Ge atoms, respectively.

Table 1 shows the volumes of amorphous Mg_xGe, Ca_xGe, Li_xGe, Na_xGe, and K_xGe with full compositions. From the equation ($[V(M_xGe) - V(Ge)]/x$), the volumes occupied by M in M_xGe were 21.76, 34.88, 13.73, 29.94, and 63.32 Å^3 for Mg_xGe, Ca_xGe, Li_xGe, Na_xGe, and K_xGe, respectively. The corresponding ratios for volume expansion (defined as $(V - V_0)/V_0 \times 100\%$) for $Mg_{2.3}Ge$ and $Ca_{2.4}Ge$ are 231% and 386% for $Mg_{2.3}Ge$ and $Ca_{2.4}Ge$, respectively, as shown in Table 2. This result indicates that the volume expansion ratio was considerably smaller for the fully magnesiated Ge alloy than for the fully calciated Ge alloy. Another noteworthy point is that $Mg_{2.3}Ge$ showed a favorably lower volume expansion ratio (231%) compared with $Li_{4.0}Ge$ (253%). However, the volume expansion of magnesiated Ge could result in capacity degradation during cycling because the discharge–charge volume expansion ratio remains high. This challenge may be overcome by advanced electrode architectures, such as nanostructures, nanopores, and composite electrodes, as demonstrated in Ge anode systems [26,61–64]. Therefore, the calculated high capacity of 1697 mA·h·g^{-1} and low volume expansion ratio of 231% in the $Mg_{2.3}Ge$ alloy suggest that $Mg_{2.3}Ge$ could be utilized as a next-generation anode material in LIBs.

Table 1. Diffusion parameters of $M_{0.5}Ge$ (M = Li, Na, K, Mg, and Ca) [a].

Carrier Ion	E_D	D_0	D
Li	0.26	1.4×10^{-3}	5.9×10^{-8}
Na	0.31	1.7×10^{-3}	1.2×10^{-8}
K	0.26	7.0×10^{-4}	2.8×10^{-9}
Mg	0.27	8.7×10^{-4}	3.0×10^{-8}
Ca	0.49	1.9×10^{-3}	1.1×10^{-11}

[a] E_D (eV), D_0 (cm^2 s^{-1}), and D (cm^2 s^{-1}) are the activation energy for diffusion, the pre-exponential factor, and the self-diffusion coefficient at T = 300 K, respectively.

Table 2. Capacities (mA h g^{-1}) and expansion ratios in volume (%), diffusivities (cm^2 s^{-1}) at x = 0.5 in M_xGe (M = Mg, Ca, Li, Na, and K) of $Li_{4.0}Ge$, $Na_{1.5}Ge$, $K_{1.2}Ge$, $Mg_{2.3}Ge$, and $Ca_{2.4}Ge$.

Carrier Ion	Capacity	Expansion Ratio	Diffusivity
Li	1476	253	5.9×10^{-8}
Na	553	207	1.2×10^{-8}
K	443	351	2.8×10^{-8}
Mg	1697	231	3.0×10^{-8}
Ca	1771	389	1.1×10^{-11}

Figure 3 shows that the decrease in the charges of Mg, Ca, and Ge is closely related to the increase in their atomic volumes in amorphous $Mg_{2.3}Ge$ and $Ca_{2.4}Ge$. These results indicate that the volume of M_xGe was determined by the total combined volume occupied by the M cations and Ge anions. The data points for Ge near −2.0 *e* are from isolated Ge–Ge pairs. While most of the Ge atoms are surrounded by the relatively larger Ca atoms with positive charges, the Ge atoms in the Ge–Ge pairs accept fewer electrons from Ca atoms, leading to the deviated data points shown in Figure 3d. The isolated host element clusters, such as the Ge–Ge pairs are usually observed in the amorphous structures with large alloying atoms [46]. We interpret the volume expansion of the amorphous M_xGe alloys as originating from (1) the ionic concentration, (2) the difference in atomic volume between M and Ge ions, and (3) the charge distribution between M and Ge ions.

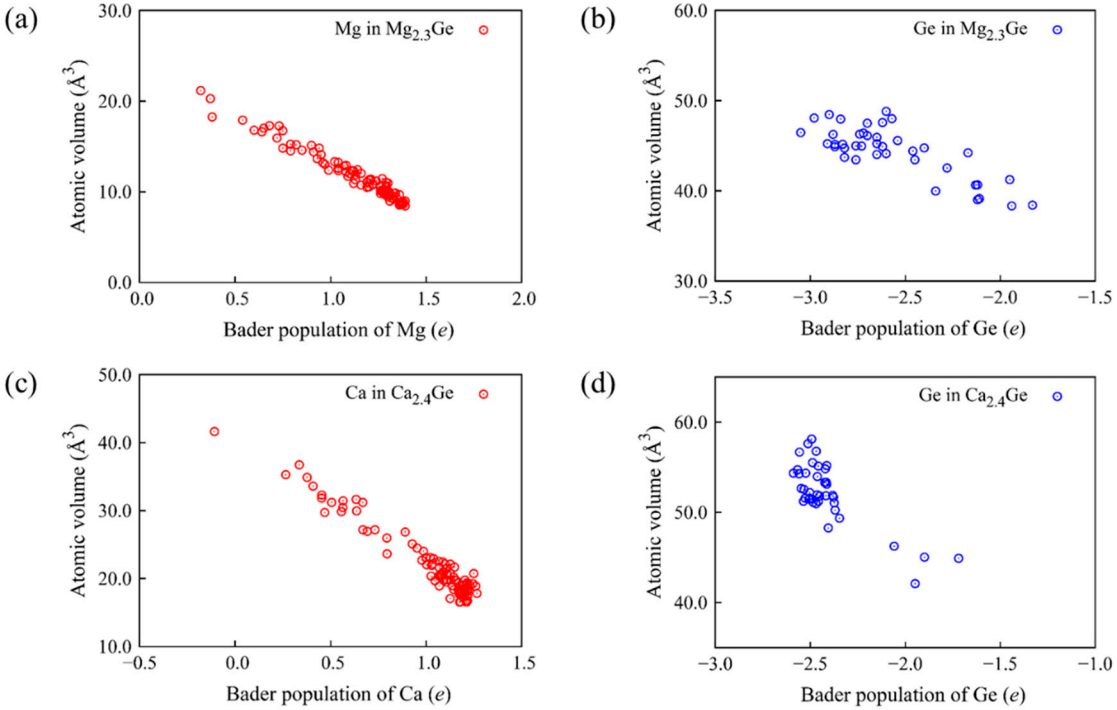

Figure 3. Relationship between atomic volume and charges for the elements (**a**) Mg and (**b**) Ge in $Mg_{2.3}Ge$ and (**c**) Ca and (**d**) Ge in $Ca_{2.4}Ge$.

We investigated the M-ion diffusivities in $M_{0.5}Ge$ amorphous alloys (M = Mg, Ca, Li, Na, and K) at T = 300 K, as shown in Table 2. Diffusivity studies using FPMD simulations can provide valuable information on the rate capability of Ge anodes in MIBs. The evaluated mean squared displacement (d_{ms}) values linearly increased with time t for both Mg and Ca ions (Figure S2), thereby precisely determining the D values at those temperatures. The Arrhenius plots for all cations show linear variations in ln(D) with respect to the inverse temperature, as shown in Figure 4. The temperatures, at which the mean square displacements were computed were chosen carefully because calculations that were too

high (i.e., above the melting point of 1211 K for Ge) could be problematic in terms of accuracy, and simulation times that were too close to room temperature could be extremely long. A further discussion is provided in the Supplementary Data section (Figure S2).

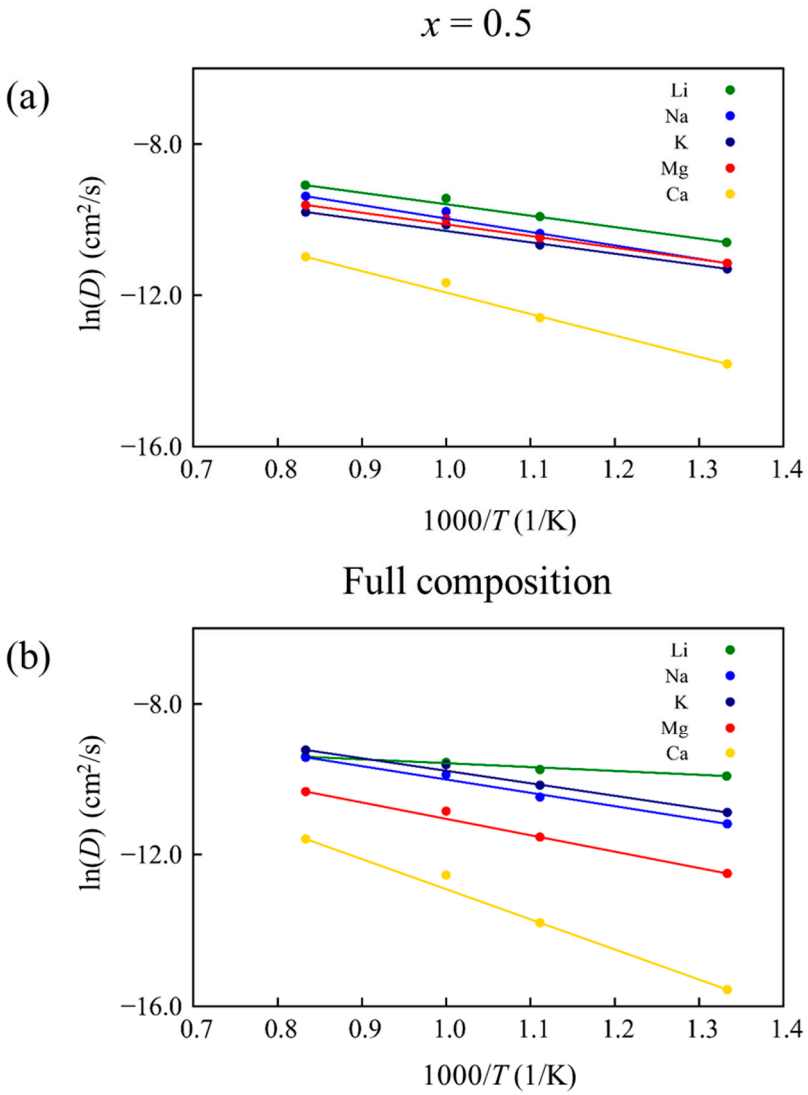

Figure 4. Logarithmic diffusivities (**a**) of carrier ions in $M_{0.5}Ge$ (M = Mg, Ca, Li, Na, and K) and (**b**) amorphous M_xGe (x = full composition).

We suggest that Mg ions diffuse considerably more rapidly than Ca ions in $M_{0.5}Ge$ alloys at room temperature. The calculated ion diffusivities (D) are 3.0×10^{-8} and 1.1×10^{-11} $cm^2 \cdot s^{-1}$ for Mg ions in $Mg_{0.5}Ge$ and Ca ions in $Ca_{0.5}Ge$ at T = 300 K, respectively, as shown in Table 1. These results indicate that the Mg ion showed a diffusivity that was three orders of magnitude superior to that of the Ca ion. Notably, Mg ion diffusion occurred at a comparable order of magnitude in $Mg_{0.5}Ge$ and in the monovalent $Li_{0.5}Ge$, $Na_{0.5}Ge$, and $K_{0.5}Ge$ alloys. This result contradicts the prevailing view that the diffusion of multivalent ions is significantly lower than that of monovalent ions, as in the Ni_2O_4, Mn_2O_4, V_2O_5, and Ti_2S_4 systems. Furthermore, the Mg ion diffusivity in amorphous Ge was even one order of magnitude superior to the Mg ion diffusivity (2.3×10^{-9} $cm^2 \cdot s^{-1}$) in $Mg_{0.5}Si$ [47]. This difference from the common understanding may be due to the structural disorder of amorphous Ge. The ion diffusivity values for amorphous $Mg_{0.5}Ge$, $Ca_{0.5}Ge$, $Li_{0.5}Ge$, $Na_{0.5}Ge$, and $K_{0.5}Ge$ are shown in Table 1, where the ion diffusivity in amorphous systems has an order of Li > Mg > K > Na >> Ca.

Table 2 summarizes the performances of amorphous Mg_xGe, Ca_xGe Li_xGe, Na_xGe, and K_xGe. The specific capacity of $Mg_{2.3}Ge$ was somewhat lower (~4%) than that of $Ca_{2.4}Ge$, which exhibited the highest capacity. However, $Mg_{2.3}Ge$ showed a relatively small volume expansion ratio (~150%) compared to $Ca_{2.4}Ge$. In addition, the Mg ions in $Mg_{2.3}Ge$ diffused more rapidly than the Ca ions in $Ca_{2.4}Ge$ by three orders of magnitude. These findings suggest that the Mg–Ge alloys have significantly better cycling performance and rate capability than Ca–Ge alloys. Table 2 summarizes the performance of M_xGe (M = Mg, Ca, Li, Na, and K), showing that (1) the order of specific capacity is Ca > Mg > Li > Na > K, (2) the volume expansion ratio has the increasing order of Na < Mg < Li < K < Ca, and (3) the order of ion transport is Li > Mg > K > Na > Ca. Compared to alloys between Ge and monovalent ions, Ge–Mg alloys showed a moderately high specific capacity, low volume expansion ratio, and fast ion transport. Accordingly, Mg^{2+} is a more promising carrier ion than Ca^{2+} for the amorphous Ge electrode in MIBs because of its superior electrochemical properties that can even compete with monovalent ions.

We attempted to relate the structural properties in $Mg_{2.3}Ge$ and $Ca_{2.4}Ge$ to their specific capacities, volume expansion ratio, and ion diffusivities. We determined the specific capacities as 1697 for Mg_xGe and 1771 $mA{\cdot}h{\cdot}g^{-1}$ for Ca_xGe from the highest concentration (x_{max} = 2.3 for Mg and 2.4 for Ca) at the most favorable formation energies as plotted in Figure 1. The detailed specific capacity (C) calculation is included in the Supporting Information. Note that x_{max} plays an important role in determining the specific capacities because both Mg_xGe and Ca_xGe have the same charge and molecular weight per structural formula unit.

We found that the highest concentrations, x_{max}, were related to the number of carrier ions that could be coordinated to the Ge host anions. The average host ion coordination numbers for $Mg_{2.3}Ge$ and $Ca_{2.4}Ge$ were $CN_{Ge–Mg}$ = 2.56 and $CN_{Ge–Ca}$ = 2.64, respectively, in line with a somewhat smaller capacity of $Mg_{2.3}Ge$ than of $Ca_{2.4}Ge$. This relationship was consistent for monovalent ions as well as for these multivalent ions. Figure 5a shows that the coordination numbers are $CN_{Ge–Li}$ = 3.62 in $Li_{4.0}Ge$, $CN_{Ge–Na}$ = 2.36 in $Na_{1.5}Ge$, and $CN_{Ge–K}$ = 1.90 in $K_{1.2}Ge$. The $CN_{Ge–M}$ (M = Mg, Ca, Li, Na, and K) values have the order Li (3.62) > Ca (2.64) > Mg (2.56) > Na (2.36) > K (1.90), which was analogous to the order of x_{max}: Li (4.0) > Ca (2.4) > Mg (2.3) > Na (1.5) > K (1.2). Considering the different n_e for monovalent ($1 \times x_{max}$) and divalent ($2 \times x_{max}$) ions, we can obtain the order of capacity (Ca > Mg > Li > Na > K) from the order of maximum ion concentrations (x_{max}). Furthermore, the CN values are $CN_{Ge–Ge}$ = 4.24 in $Mg_{2.3}Ge$ and $CN_{Ge–Ge}$ = 0.71 in $Ca_{2.4}Ge$, as shown in Figure 5b. This result indicates that the Mg–Ge bond was weaker than the Ca–Ge bond and should result in rapid Mg ion transport in the Mg–Ge alloy.

The relationship between the volume extension ratios and the volumes accommodated by the M ions in M_xGe was also analyzed in terms of the x_{max} values. While the ion concentrations at the maximum charging for Mg_xGe (x_{max} = 2.3) and Ca_xGe (x_{max} = 2.4) were similar, a noticeable difference was observed in the volumes accommodated by Mg and Ca at 21.76 for Mg and 34.88 $Å^3$ for Ca, resulting in a considerably lower volume expansion ratio of 231% for $Mg_{2.3}Ge$ compared to 386% for $Ca_{2.4}Ge$. The contrasting difference in the volumes accommodated by Mg and Ca may originate from the difference in the atomic radii between Mg (1.50 Å) and Ca (1.80 Å). Notably, we found that the order of the volume occupied by M in M_xGe (M = Mg, Ca, Li, Na, and K) was K (63.32 $Å^3$) > Ca (34.88 $Å^3$) > Na (29.94 $Å^3$) > Mg (21.76 $Å^3$) > Li (13.73 $Å^3$), which was consistent with the order of the atomic radii: K (2.20) > Ca (1.80) ≈ Na (1.80) > Mg (1.50) > Li (1.45 Å).

Ion transport in amorphous alloys is a complicated process that is affected by the interaction between the carrier ions, the host ions, and the local structures [46,47]. In particular, the ion–host interaction, indicative of the M–Ge attraction (M = Mg, Ca, Li, Na, and K), appeared to be the primary reason for the considerably quicker ion diffusion in $Mg_{0.5}Ge$ (3.03×10^{-8} $cm^2{\cdot}s^{-1}$) than in $Ca_{0.5}Ge$ (1.13×10^{-11} $cm^2{\cdot}s^{-1}$). A weaker interaction between the carrier ions and the host ions creates conditions where ions can more easily break ion–host bonds and travel through the host structure. The strength of the M–Ge

bond seemed to be related to the coordination number of Ge ($CN_{Ge–Ge}$) in M_xGe at x = 0.5. The $CN_{Ge–Ge}$ values (Figure 6) might indicate the weakness of the M–Ge bond, as a weak ion–Ge bond may prevent ions from breaking the Ge–Ge bond, allowing extra Ge–Ge bonds in the system. The coordination numbers were $CN_{Ge–Ge}$ = 1.58 in $Mg_{0.5}Ge$ and $CN_{Ge–Ge}$ = 0.96 in $Ca_{0.5}Ge$, implying that the Mg–Ge bond was weaker than the Ca–Ge bond. This weak Mg–Ge bond can facilitate the diffusion of Mg ions.

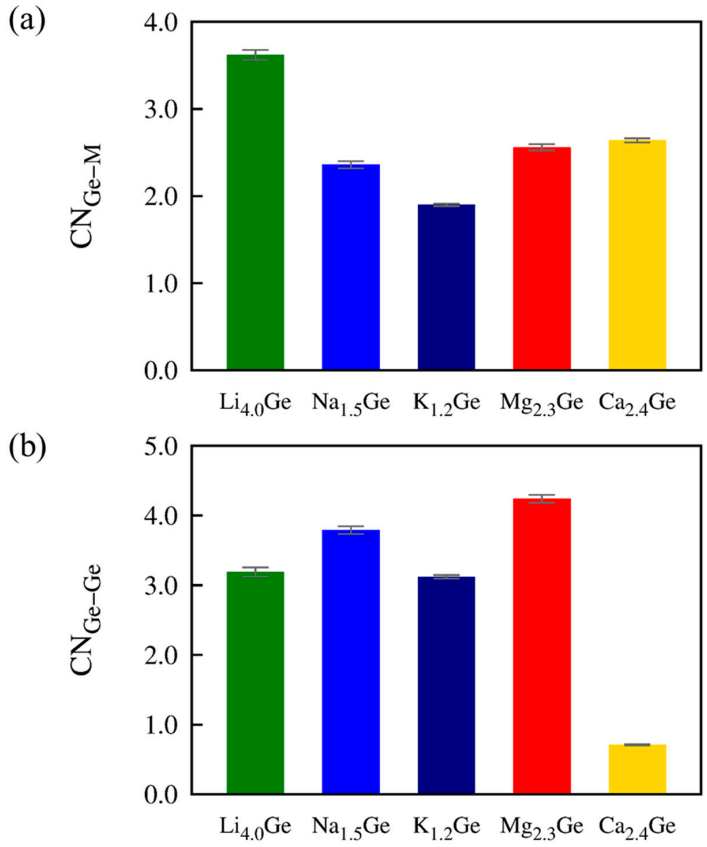

Figure 5. Average partial CN values of Ge in M_xGe (M= Mg, Ca, Li, Na, and K) (x = maximum concentration). (**a**) $CN_{Ge–M}$ and (**b**) $CN_{Ge–Ge}$. Cutoff distances for the nearest bond are 2.64, 3.11, 3.48, 2.79, 3.68, and 4.50 Å for Ge–M (M = Mg, Ca, Li, Na, and K) and Ge–Ge pairs, respectively (Figure S3 in the Supplementary data).

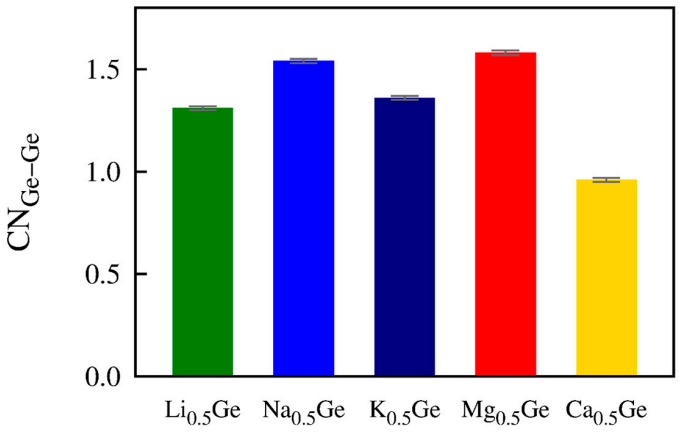

Figure 6. Average partial coordination numbers of Ge–Ge pairs in $M_{0.5}Ge$ (M= Mg, Ca, Li, Na, and K). The cutoff distances for the nearest bond are 2.64, 3.11, 3.48, 2.79, and 3.68 Å for Ge–Ge (M = Mg, Ca, Li, Na, and K) pairs, respectively.

The relationship between the M–Ge bond strength (M = Mg, Ca, Li, Na, and K) and the coordination number of $CN_{Ge–Ge}$ could be applied to monovalent ion cases. The coordination numbers of $CN_{Ge–Ge}$ were 1.58, 0.96, 1.31, 1.54, and 1.36 in Mg_xGe, Ca_xGe, Li_xGe, Na_xGe, and K_xGe (x = 0.5), respectively, implying that the bond strength of M–Ge (M = Mg, Ca, Li, Na, and K) follows the order of Ca > Li > K > Na ~ Mg, consistent with the order of the thermodynamic driving forces for alloy formation (Ca > Li > K > Mg > Na). Assuming that the interaction between ion and host atoms is the primary factor that determines the formation energy of M_xGe, the observed analogous trends strongly support the discussion that the strength of the bond between ion and host Ge atoms is highly correlated with the $CN_{Ge–Ge}$ values. Along with the aforementioned discussion on $CN_{Ge–M}$, we conclude that the $CN_{host–host}$ and $CN_{host–ion}$ values can be used as important indicators for evaluating the electrochemical performance of alloy-based anode materials, including the formation energy, specific capacity, volume expansion ratio, and ion diffusivity.

4. Conclusions

By investigating multivalent ions such as Al^{3+}, Mg^{2+}, Ca^{2+}, Zn^{2+}, and using first-principles calculations, we demonstrated that Mg^{2+} and Ca^{2+} can work stably as multivalent carrier ions for amorphous Ge anodes. Furthermore, Mg^{2+} has better cycle stability and rate capability than Ca^{2+}. Specifically, $Mg_{2.3}Ge$ demonstrates a capacity of 1697 $mA{\cdot}h{\cdot}g^{-1}$, a volume expansion ratio of 231%, and an ion diffusivity of 3.0×10^{-8} $cm^2{\cdot}s^{-1}$; these values are equivalent to or superior to those of $Li_{4.0}Ge$, $Na_{1.5}Ge$, and $K_{1.2}Ge$. The strong correlation between the electrochemical performance and structural properties of Ge alloys with monovalent and multivalent ions offers comprehensive insight into alloying mechanisms. The findings of this study suggest that Ge anodes could be used in practical multivalent-ion batteries, as Mg^{2+} emerged as the most promising multivalent ion for amorphous Ge anodes and showed comparable or even better performance than traditional monovalent ions. Moreover, we also found that the CN values of the host atoms ($CN_{host–host}$) and ions ($CN_{host–ion}$) can be used to understand the relationship between the structural properties and electrochemical performance of alloying anode materials. The results presented here will serve as a helpful reference for experimental researchers working on the development of alloying anode materials for multivalent-ion batteries. Moreover, our results demonstrate a new class of materials that can overcome the skyrocketing demands for battery capacities while also revealing an effective theoretical methodology for the development of alloying electrodes, which are among the most promising electrode materials for next-generation batteries [65,66].

Supplementary Materials: The following supporting information can be downloaded at: https://www.mdpi.com/article/10.3390/nano13212868/s1, Figure S1: Temperature and energy changes during the FPMD simulation of $Mg_{2.3}Ge$; Figure S2: Mean squared displacements for Mg and Ca atoms; Figure S3: Partial radial distribution functions g(r) for Ge–Ge pairs; Figure S4: Average partial coordination numbers, $CN_{Ge–M}$; Figure S5: The average voltage of M_xGe; Table S1: Atomic coordinates of Mg and Ge atoms in $Mg_{2.3}Ge$; Table S2: Atomic coordinates of Ca and Ge atoms in $Ca_{2.4}Ge$. Refs. [37,45,46,49,67] are cited in Supplementary Materials.

Author Contributions: Conceptualization, S.L.; investigation, C.K. and U.H.; data curation, C.K. and U.H.; writing—original draft, C.K. and U.H.; writing—review and editing, S.L. and Y.-K.H.; supervision, S.L. and Y.-K.H.; funding acquisition, Y.-K.H. All authors have read and agreed to the published version of the manuscript.

Funding: This research was supported by Basic Science Research Program through the National Research Foundation of Korea (NRF) funded by the Ministry of Education (NRF-2021R1F1A1046600) and the R&D program (C3-2411) funded by the Korea Institute of Energy Research (KIER). We also acknowledge the support for supercomputing resources from the Supercomputing Center/KISTI (KSC-2019-INO-0003).

Data Availability Statement: The data that support the findings of this study are available from the corresponding authors upon reasonable request.

Conflicts of Interest: The authors declare no conflict of interest.

References

1. Deng, W.; Liu, W.; Zhu, H.; Chen, L.; Liao, H.; Chen, H. Click-chemistry and ionic cross-linking induced double cross-linking ionogel electrolyte for flexible lithium-ion batteries. *J. Energy Storage* **2023**, *72*, 108509.
2. Li, L.; Nam, J.S.; Kim, M.S.; Wang, Y.; Jiang, S.; Hou, H.; Kim, I.-D. Sulfur–Carbon Electrode with PEO-LiFSI-PVDF Composite Coating for High-Rate and Long-Life Lithium–Sulfur Batteries. *Adv. Energy Mater.* **2023**, *13*, 2302139. [CrossRef]
3. Deng, W.-N.; Li, Y.-H.; Xu, D.-F.; Zhou, W.; Xiang, K.-X.; Chen, H. Three-dimensional hierarchically porous nitrogen-doped carbon from water hyacinth as selenium host for high-performance lithium–selenium batteries. *Rare Met.* **2022**, *41*, 3432–3445. [CrossRef]
4. Wen, X.; Luo, J.; Xiang, K.; Zhou, W.; Zhang, C.; Chen, H. High-performance monoclinic WO_3 nanospheres with the novel NH^{4+} diffusion behaviors for aqueous ammonium-ion batteries. *Chem. Eng. J.* **2023**, *458*, 141381. [CrossRef]
5. Deng, W.; Xu, Y.; Zhang, X.; Li, C.; Liu, Y.; Xiang, K.; Chen, H. $(NH_4)_2Co_2V_{10}O_{28}\cdot 16H_2O/(NH_4)_2V_{10}O_{25}\cdot 8H_2O$ heterostructure as cathode for high-performance aqueous Zn-ion batteries . *J. Alloys Compd.* **2022**, *903*, 163824. [CrossRef]
6. Guo, Z.; Han, X.; Zhang, C.; He, S.; Liu, K.; Hu, J.; Yang, W.; Jian, S.; Jiang, S.; Duan, G. Activation of biomass-derived porous carbon for supercapacitors: A review. *Chin. Chem. Lett.* **2023**, in press. [CrossRef]
7. Xiao, J.; Li, H.; Zhang, H.; He, S.; Zhang, Q.; Liu, K.; Jiang, S.; Duan, G.; Zhang, K. Nanocellulose and its derived composite electrodes toward supercapacitors: Fabrication, properties, and challenges. *J. Bioresour. Bioprod.* **2022**, *7*, 245–269.
8. Wei, C.; Tan, L.; Zhang, Y.; Wang, Z.; Feng, J.; Qian, Y. Towards better Mg metal anodes in rechargeable Mg batteries: Challenges, strategies, and perspectives. *Energy Storage Mater.* **2022**, *52*, 299–319.
9. Huang, W.; Zhang, K.; Yuan, B.; Yang, L.; Zhu, M. Predominant intercalation of H^+ enables ultrahigh rate capability of oxygen deficient MoO_3 for aqueous Al-ion batteries. *Energy Storage Mater.* **2022**, *50*, 152–160. [CrossRef]
10. Yaghoobnejad Asl, H.; Manthiram, A. Mass Transfer of Divalent Ions in an Oxide Host: Comparison of Mg^{2+} and Zn^{2+} Diffusion in Hexagonal $K_xW_3O_9$ Bronze. *Chem. Mater.* **2019**, *31*, 2296–2307. [CrossRef]
11. Chen, Y.; Fan, K.; Gao, Y.; Wang, C. Challenges and Perspectives of Organic Multivalent Metal-Ion Batteries. *Adv. Mater.* **2022**, *34*, 2200662. [CrossRef]
12. Wang, Z.; Li, Y.; Wang, J.; Ji, R.; Yuan, H.; Wang, Y.; Wang, H. Recent progress of flexible aqueous multivalent ion batteries. *Carbon Energy* **2022**, *4*, 411–445. [CrossRef]
13. Zhang, W.; Dai, Y.; Chen, R.; Xu, Z.; Li, J.; Zong, W.; Li, H.; Li, Z.; Zhang, Z.; Zhu, J.; et al. Highly Reversible Zinc Metal Anode in a Dilute Aqueous Electrolyte Enabled by a pH Buffer Additive. *Angew. Chem. Int. Ed.* **2022**, *62*, e202212695. [CrossRef]
14. Zhang, X.; Wei, H.; Ren, B.; Jiang, J.; Qu, G.; Yang, J.; Chen, G.; Li, H.; Zhi, C.; Liu, Z. Unlocking High-Performance Ammonium-Ion Batteries: Activation of In-Layer Channels for Enhanced Ion Storage and Migration. *Adv. Mater.* **2023**, *35*, 2304209. [CrossRef]
15. Yang, X.; Zhang, C.; Chai, L.; Zhang, W.; Li, Z. Bimetallic Rechargeable Al/Zn Hybrid Aqueous Batteries Based on Al–Zn Alloys with Composite Electrolytes. *Adv. Mater.* **2022**, *34*, 2206099. [CrossRef]
16. Li, J.; Han, C.; Ou, X.; Tang, Y. Concentrated Electrolyte for High-Performance Ca-Ion Battery Based on Organic Anode and Graphite Cathode. *Angew. Chem. Int. Ed.* **2022**, *134*, e202116668. [CrossRef]
17. Xiao, X.; Zheng, Z.; Zhong, X.; Gao, R.; Piao, Z.; Jiao, M.; Zhou, G. Rational Design of Flexible Zn-Based Batteries for Wearable Electronic Devices. *ACS Nano* **2023**, *17*, 1764–1802. [CrossRef]
18. Zhao, S.; Li, C.; Zhang, X.; Li, N.; Wang, T.; Li, X.; Wang, C.; Qu, G.; Xu, X. An advanced Ca/Zn hybrid battery enabled by the dendrite-free zinc anode and a reversible calcification/decalcification NASICON cathode. *Sci. Bull.* **2023**, *68*, 56–64. [CrossRef]
19. Shi, F.; Chen, C.; Xu, Z.-L. Recent Advances on Electrospun Nanofiber Materials for Post-lithium Ion Batteries. *Adv. Fiber Mater.* **2021**, *3*, 275–301. [CrossRef]
20. Wei, Y.; Wang, Z.; Wu, J.; Liu, B.; Zhang, Y.; Huang, S. Effect of Oxygen Vacancies and F-Doping on TiO_2(B) as Anode for Mg-Ion Batteries. *J. Phys. Chem. C* **2023**, *127*, 14086–14097. [CrossRef]
21. Li, W.; Ma, Y.; Shi, H.; Jiang, K.; Wang, D. Cu_7Te_4 as an Anode Material and Zn Dendrite Inhibitor for Aqueous Zn-Ion Battery. *Adv. Funct. Mater.* **2022**, *32*, 2205602. [CrossRef]
22. Zhu, X.; Yang, Y.; Shu, X.; Xu, T.; Jing, Y. Computational insights into the rational design of organic electrode materials for metal ion batteries. *Comput. Mol. Sci.* **2023**, *13*, e1660. [CrossRef]
23. Xie, Y.; Duan, C.; Yang, Z.; Feng, Y.; Yao, J. Post-treatment of ZIF-67/Ni_3S_4 Nanoparticle Composites by Metal Ions and Solvent-Assisted Etching as Advanced Electrodes for Supercapacitors. *ACS Appl. Nano Mater.* **2023**, *6*, 12105–12113. [CrossRef]
24. Liu, H.; Wu, T.; Zhang, L.; Wang, X.; Li, H.; Liu, S.; Zhang, Q.; Zhang, X.; Yu, H. Germanium Nanowires via Molten-Salt Electrolysis for Lithium Battery Anode. *ACS Nano* **2022**, *16*, 14402–14411. [CrossRef]
25. Jo, C.; Wen, B.; Jeong, H.; Park, S.K.; Son, Y.; Volder, M.D. Spinodal Decomposition Method for Structuring Germanium–Carbon Li-Ion Battery Anodes. *ACS Nano* **2023**, *17*, 8403–8410. [CrossRef] [PubMed]
26. Huang, J.-Q.; Guo, X.; Huang, J.; Tan, H.; Du, X.; Zhu, Y.; Zhang, B. Critical roles of microstructure and interphase on the stability of microsized germanium anode. *J. Power Sources* **2021**, *481*, 228916. [CrossRef]
27. Wang, Y.; Luo, S.; Chen, M.; Wu, L. Uniformly Confined Germanium Quantum Dots in 3D Ordered Porous Carbon Framework for High-Performance Li-ion Battery. *Adv. Funct. Mater.* **2020**, *30*, 2000373. [CrossRef]

28. Zhang, C.; Lin, Z.; Yang, Z.; Xiao, D.; Hu, P.; Xu, H.; Duan, Y.; Pang, S.; Gu, L.; Cui, G. Hierarchically Designed Germanium Microcubes with High Initial Coulombic Efficiency toward Highly Reversible Lithium Storage. *Chem. Mater.* **2015**, *27*, 2189–2194. [CrossRef]
29. Liu, Q.; Hou, J.; Xu, C.; Chen, Z.; Qin, R.; Liu, H. TiO_2 particles wrapped onto macroporous germanium skeleton as high performance anode for lithium-ion batteries. *Chem. Eng. J.* **2020**, *381*, 122649. [CrossRef]
30. Mo, R.; Rooney, D.; Sun, K. Hierarchical graphene-scaffolded mesoporous germanium dioxide nanostructure for high-performance flexible lithium-ion batteries. *Energy Storage Mater.* **2020**, *29*, 198–206. [CrossRef]
31. Ngo, D.T.; Le, H.T.T.; Kim, C.; Lee, J.-Y.; Fisher, J.G.; Kim, I.-D.; Park, C.-J. Mass-scalable synthesis of 3D porous germanium–carbon composite particles as an ultra-high rate anode for lithium ion batteries. *Energy Environ. Sci.* **2015**, *8*, 3577–3588. [CrossRef]
32. Li, P.; Zhang, H.; Meng, L.; Ding, Y.; Wang, J.; Lou, X.; Bai, H. In Situ Synthesis of Germanium Particles Decorated in Conjugated N-doped Carbon Matrix: Boosting the Performance of the Lithium-Ion Battery. *ACS Appl. Energy Mater.* **2022**, *6*, 362–370. [CrossRef]
33. Metcalf, T.H.; Liu, X.; Jernigan, G.; Culbertson, J.C.; Abernathy, M.; Molina-Ruiz, M.; Hellman, F. Internal friction measurements of low energy excitations in amorphous germanium thin films. *J. Alloys Compd.* **2021**, *856*, 157616. [CrossRef]
34. Liu, X.; Wu, X.-Y.; Chang, B.; Wang, K.-X. Recent progress on germanium-based anodes for lithium ion batteries: Efficient lithiation strategies and mechanisms. *Energy Storage Mater.* **2020**, *30*, 146–169. [CrossRef]
35. Chou, C.-Y.; Hwang, G.S. On the origin of the significant difference in lithiation behavior between silicon and germanium. *J. Power Sources* **2014**, *263*, 252–258. [CrossRef]
36. Kohandehghan, A.; Cui, K.; Kupsta, M.; Ding, J.; Memarzadeh Lotfabad, E.; Kalisvaart, W.P.; Mitlin, D. Activation with Li Enables Facile Sodium Storage in Germanium. *Nano Lett.* **2014**, *14*, 5873–5882. [CrossRef]
37. Jung, S.C.; Jung, D.S.; Choi, J.W.; Han, Y.-K. Atom-Level Understanding of the Sodiation Process in Silicon Anode Material. *J. Phys. Chem. Lett.* **2014**, *5*, 1283–1288. [CrossRef]
38. Jung, S.C.; Kim, H.-J.; Kang, Y.-J.; Han, Y.-K. Advantages of Ge anode for Na-ion batteries: Ge vs. Si and Sn. *J. Alloys Compd.* **2016**, *688*, 158–163. [CrossRef]
39. Lu, X.; Adkins, E.R.; He, Y.; Zhong, L.; Luo, L.; Mao, S.X.; Wang, C.-M.; Korgel, B.A. Germanium as a Sodium Ion Battery Material: *In Situ* TEM Reveals Fast Sodiation Kinetics with High Capacity. *Chem. Mater.* **2016**, *28*, 1236–1242. [CrossRef]
40. Liu, J.; Muhammad, S.; Wei, Z.; Zhu, J.; Duan, X. Hierarchical N-doping germanium/carbon nanofibers as anode for high-performance lithium-ion and sodium-ion batteries. *Nanotech.* **2019**, *31*, 015402. [CrossRef]
41. Wu, F.; Yang, H.; Bai, Y.; Wu, C. Paving the path toward reliable cathode materials for aluminum-ion batteries. *Adv. Mater.* **2019**, *31*, 1806510. [CrossRef]
42. Liu, Z.; Qin, L.; Cao, X.; Zhou, J.; Pan, A.; Fang, G.; Wang, S.; Liang, S. Ion migration and defect effect of electrode materials in multivalent-ion batteries. *Prog. Mater. Sci.* **2022**, *125*, 100911. [CrossRef]
43. Liu, C.; Jiang, Y.; Meng, C.; Liu, X.; Li, B.; Xia, S. Amorphous Germanium Nanomaterials as High-Performance Anode for Lithium and Sodium-Ion Batteries. *Adv. Mater. Technol.* **2023**, *8*, 2201817. [CrossRef]
44. Hüger, E.; Strauß, F.; Stahn, J.; Deubener, J.; Bruns, M.; Schmidt, H. In-situ Measurement of Self-Atom Diffusion in Solids Using Amorphous Germanium as a Model System. *Sci. Rep.* **2018**, *8*, 17607. [CrossRef] [PubMed]
45. Jung, S.C.; Choi, J.W.; Han, Y.-K. Anisotropic volume expansion of crystalline silicon during electrochemical lithium insertion: An atomic level rationale. *Nano Lett.* **2012**, *12*, 5342–5347. [CrossRef]
46. Lee, S.; Jung, S.C.; Han, Y.-K. First-principles molecular dynamics study on ultrafast potassium ion transport in silicon anode. *J. Power Sources* **2019**, *415*, 119–125. [CrossRef]
47. Lee, S.; Ko, M.; Jung, S.C.; Han, Y.-K. Silicon as the Anode Material for Multivalent-Ion Batteries: A First-Principles Dynamics Study. *ACS Appl. Mater. Interfaces* **2020**, *12*, 55746–55755. [CrossRef]
48. Jung, S.C.; Han, Y.-K. How Do Li Atoms Pass through the Al_2O_3 Coating Layer during Lithiation in Li-ion Batteries? *J. Phys. Chem. Lett.* **2013**, *4*, 2681–2685. [CrossRef]
49. Jung, S.C.; Kim, H.-J.; Choi, J.W.; Han, Y.-K. Sodium Ion Diffusion in Al_2O_3: A Distinct Perspective Compared with Lithium Ion Diffusion. *Nano Lett.* **2014**, *14*, 6559–6563. [CrossRef]
50. Lee, S.W.; McDowell, M.T.; Choi, J.W.; Cui, Y. Anomalous Shape Changes of Silicon Nanopillars by Electrochemical Lithiation. *Nano Lett.* **2011**, *11*, 3034–3039. [CrossRef]
51. Aaltonen, T.; Nilsen, O.; Magrasó, A.; Fjellvåg, H. Atomic Layer Deposition of Li_2O–Al_2O_3 Thin Films. *Chem. Mater.* **2011**, *23*, 4669–4675. [CrossRef]
52. Han, X.; Liu, Y.; Jia, Z.; Chen, Y.-C.; Wan, J.; Weadock, N.; Gaskell, K.J.; Li, T.; Hu, L. Atomic-Layer-Deposition Oxide Nanoglue for Sodium Ion Batteries. *Nano Lett.* **2014**, *14*, 139–147. [CrossRef] [PubMed]
53. Jarolimek, K.; Hazrati, E.; de Groot, R.A.; de Wijs, G.A. Band Offsets at the Interface between Crystalline and Amorphous Silicon from First Principles. *Phys. Rev. Appl.* **2017**, *8*, 014026. [CrossRef]
54. Jarolimek, K.; de Groot, R.A.; de Wijs, G.A.; Zeman, M. First-principles study of hydrogenated amorphous silicon. *Phys. Rev. B* **2009**, *79*, 155206. [CrossRef]
55. Pulay, P. Convergence acceleration of iterative sequences. The case of SCF iteration. *Chem. Phys. Lett.* **1980**, *73*, 393–398. [CrossRef]
56. Lewis, L.J. Fifty years of amorphous silicon models: The end of the story? *J. Non-Cryst. Solids* **2022**, *580*, 121383. [CrossRef]

57. Dalba, G.; Fornasini, P.; Grazioli, M.; Rocca, F. Local disorder in crystalline and amorphous germanium. *Phys. Rev. B* **1995**, *52*, 11034. [CrossRef]
58. Qian, L.; Chen, J.F.; Li, Y.H.; Wu, L.; Wang, H.F.; Chen, A.P.; Hu, P.; Zheng, L.R.; Yang, H.G. Orange Zinc Germanate with Metallic Ge–Ge Bonds as a Chromophore-Like Center for Visible-Light-Driven Water Splitting. *Angew. Chem.* **2015**, *127*, 11629–11633. [CrossRef]
59. Rao, Y.K.; Belton, G.R. Thermodynamic properties of Mg−Ge alloys. *Metall. Trans.* **1971**, *2*, 2215–2219. [CrossRef]
60. Palenzona, A.; Manfrinetti, P.; Fornasini, M.L. The phase diagram of the Ca–Ge system. *J. Alloys Compd.* **2002**, *345*, 144–147. [CrossRef]
61. Yan, Y.; Liu, Y.; Zhang, Y.; Qin, C.; Yu, H.; Bakenov, Z.; Wang, Z. Sn modified nanoporous Ge for improved lithium storage performance. *J. Colloid Interface Sci.* **2021**, *602*, 563–572. [CrossRef] [PubMed]
62. Chen, Y.; Zou, Y.; Shen, X.; Qiu, J.; Lian, J.; Pu, J.; Li, S.; Du, F.-H.; Li, S.-Q.; Ji, Z.; et al. Ge nanoparticles uniformly immobilized on 3D interconnected porous graphene frameworks as anodes for high-performance lithium-ion batteries. *Energy Chem.* **2022**, *69*, 161–173. [CrossRef]
63. Fang, S.; Tong, Z.; Zhang, X. 3D nitrogen-doped carbon foam supported Ge@C composite as anode for high performance lithium-ion battery. *Chem. Eng. J.* **2017**, *322*, 188–195. [CrossRef]
64. Kennedy, T.; Brandon, M.; Ryan, K.M. Advances in the application of silicon and germanium nanowires for high-performance lithium-ion batteries. *Adv. Mater.* **2016**, *28*, 5696–5704. [CrossRef]
65. Chen, Z.; Soltani, A.; Chen, Y.; Zhang, Q.; Davoodi, A.; Hosseinpour, S.; Peukert, W.; Liu, W. Emerging Organic Surface Chemistry for Si Anodes in Lithium-Ion Batteries: Advances, Prospects, and Beyond. *Adv. Energy Mater.* **2022**, *12*, 2200924. [CrossRef]
66. Liu, H.; Sun, Q.; Zhang, H.; Cheng, J.; Li, Y.; Zeng, Z.; Zhang, S.; Xu, X.; Ji, F.; Li, D.; et al. The application road of silicon-based anode in lithium-ion batteries: From liquid electrolyte to solid-state electrolyte. *Energy Storage Mater.* **2023**, *55*, 244–263. [CrossRef]
67. Jung, S.C.; Choi, J.-H.; Han, Y.-K. The origin of excellent rate and cycle performance of Sn_4P_3 binary electrodes for sodium-ion batteries. *J. Mater. Chem. A* **2018**, *6*, 1772–1779. [CrossRef]